Rock and Soil Mechanics 2026 47(1): 323−336 ISSN 1000−7598
https: //doi.org/10.26599/RSM.2025.94300001 journal homepage: rocksoilmech.whrsm.ac.cn

Genetic algorithm-optimized back propagation neural network for the characterization of backward erosion piping channels

LIANG Yue[1, 2, 3], RAO Yu-feng[1], ZHAO Zhuo-yue[4], XU Bin [1, 2, 3], YANG Xiao-xia[1], XIA Ri-feng[1], DENG Hui-dan[1], RASHID Hafiz Aqib[1]

1. The College of River and Ocean Engineering, Chongqing Jiaotong University, Chongqing 400074, China;

2. National Engineering Research Center for Inland Waterway Regulation, Chongqing Jiaotong University, Chongqing 400074, China;

3. Key Laboratory of Hydraulic and Waterway Engineering of Ministry of Education, Chongqing Jiaotong University, Chongqing 400074, China;

4. CCCC - FHDI Engineering Co., Ltd., Guangzhou Guangdong 510230, China

Abstract: The use of levees is one of the most prevalent and effective strategies for flood protection. However, owing to the ageing of levees, inconsistent reinforcement efforts, and complex geological conditions, hazards such as piping frequently arise during flood seasons, which lead to significant and often irreparable damage. This study investigates backward erosion piping (BEP) in the foundations of double-structured levees via a back-propagation (BP) neural network optimized by a genetic algorithm (GA). The primary contributions of this study include: 1) the construction of a training dataset through numerical simulations of BEP in heterogeneous aquifers and validation of the dataset against laboratory sandbox piping tests to verify its reliability; 2) the extraction of head H and permeability coefficient K data from Groups II, III, and IV in the BEP laboratory tests, augmentation of the dataset, and optimization of the GA–BP model to characterize test results in Group I, where the results demonstrate that the optimized model more accurately characterizes areas where the $K \leqslant 1.0$ cm/s; and 3) the use of the optimized GA-BP model to characterizes the development of a BEP channel. The results indicate that the model accurately captures the general trends. However, minor discrepancies remain in the characterized channel location and size compared with the actual conditions. In conclusion, this study offers an effective tool for characterizing BEP and demonstrates the potential of the GA–BP network model for practical applications in this field.

Keywords: backward erosion piping; piping channel; back propagation neural network; genetic algorithm; permeability coefficient

1 Introduction

Levees as crucial hydraulic engineering facilities, play an irreplaceable role in flood prevention and disaster mitigation. Their stability directly affects the safety and property of nearby residents, as well as their overall social stability[1]. By the end of 2023, China had constructed over 400,000 kilometers of levees across coastal and inland regions, thereby safeguarding countless residents and economic assets[2]. Despite these extensive efforts, significant challenges remain. One of the most pressing issues is backward erosion piping (BEP), which continues to pose a serious threat to the integrity of levees[3]. BEP refers to the gradual removal of granular material from the foundation of a dam or levee due to water flow[4-6]. Under the influence of flowing water, this material is progressively dislodged, which leads to the formation of shallow pipes that develop in the opposite direction of the water flow. This process can ultimately result in the failure of water-retaining structures[7]. Consequently, BEP is considered one of the most critical failure mechanisms for dikes and levees, and it is a primary cause of levee failure. According to the Ministry of Water Resources of China (MWR), hundreds of piping incidents occur nationwide each year and are mostly concentrated during peak flood seasons[8]. For example, in July 2024, a BEP incident occurred at the Tuanzhouwan levee in Huarong County, Hu'nan, China, which resulted in the release of approximately 200 million cubic meters of floodwater; this necessitated the emergency evacuation of 7,680 residents and severely disrupted local socioeconomic conditions and livelihoods[9]. The occurrence and progression of BEP are highly random and difficult to detect, thus posing significant challenges for traditional monitoring and early warning systems. Therefore, the development and implementation of advanced technologies to enhance BEP monitoring and early warning capabilities are of urgent necessity to more effectively safeguard lives and property[10].

Geophysical investigation is a common method for detecting BEP. For example, Loperte et al.[11] used ground-penetrating radar (GPR) to monitor and

Received: 08 January 2025 Accepted: 31 July 2025
This work was supported by the Natural Science Foundation of China (52379097, 52509138), the Guangxi Science and Technology Program (GuiKe AA23062023), the Graduate Scientific Research and Innovation Foundation of Chongqing Jiaotong University (2025S0028), the Chongqing Water Conservancy Technology Project (CQSLK-2024005) and the Science and Technology Research Program of Chongqing Municipal Education Commission (KJQN202300744).
First author: LIANG Yue, male, born in 1985, PhD, Professor, mainly engaged in teaching and research on the mechanism and prevention of hydraulic disasters. E-mail: liangyue2560@163.com
Corresponding author: RAO Yu-feng, male, born in 2001, Master's student, focusing on mechanism and prevention of hydraulic disasters. E-mail: ryfeng263643@163.com

diagnose one of the largest dams in the Licata region of Brazil and successfully detected and localized subsurface sandstone embankments. Zhang et al.[12] integrated geomagnetic, high-density resistivity, and microseismical methods for comprehensive and localized fine detection of levee leakage zones. Zhao et al.[13] utilized the parallel electrical method to determine the leakage channel direction of dams. This method was also combined with the transient electromagnetic method to detect hidden dangers in the dam shoulder. Ge et al.[14] obtained geophysical survey results along the dam axis via three methods, namely electrical resistivity tomography (ERT), GPR, and surface wave analysis, and examined their differences, classified the soil and bedrock layers, and localized leakage zones. The tracing method is another approach for locating erosion channels. Qiu et al.[15] conducted temperature logging, natural tracer electric logging, and salt (NaCl) artificial tracer tests in boreholes within the hazard zone of a dam. Hamlyn et al.[16] used ERT and induced polarization methods to investigate dam infrastructure, identify potential leakage paths and provide key data for repairs. Lin et al.[17] employed ERT to detect anomalous seepage paths in earth dams and assess soil compaction levels to ensure the structural stability of the dams.

Although the geophysical methods mentioned above can effectively detect potential seepage and piping channels in dams and their foundations under specific conditions, the significant heterogeneity in geological and hydrological conditions makes it difficult to accurately distinguish between stratigraphic variations caused by natural heterogeneity and those associated with piping risks, leading to considerable uncertainty and potential misinterpretation in the detection results[18]. Furthermore, the lack of a quantitative relationship between monitoring data and the evolution of piping processes hampers the rapid and accurate localization of piping channels and the realization of real-time early warning[19-21]. Therefore, traditional methods still exhibit clear limitations in terms of precise identification, dynamic monitoring, and model generalization capabilities.

Against this background, the introduction of artificial intelligence technologies, especially neural networks, has provided new approaches for recognizing complex nonlinear features. For example, Zhai et al. [22] constructed a support vector machine classification model based on radial basis functions to identify the likelihood of piping occurrence in embankments; Rao et al.[23] compared the performance of deep belief networks (DBN), Backpropagation (BP) neural networks, and support vector machines (SVM) in identifying piping hazards; Lu et al.[24] extracted piping features from experimentally collected piping images using the YOLO model, which were then input into a multi-weight neural network to achieve classification and recognition of embankment piping disasters; Band et al.[25] developed a piping erosion model for the Zarandieh watershed in Markazi Province, Iran, based on random forest (RF), support vector machine (SVM), and Bayesian generalized linear models. These studies combine machine learning with embankment piping prediction, achieving efficient forecasting of piping and providing a basis for embankment risk assessment. These research outcomes demonstrate that neural networks show promising potential in addressing complex nonlinear problems and assisting in backward erosion piping (BEP) risk identification.

This study proposes a genetic algorithm-optimized backpropagation neural network (GA-BP) model[26-28]. The model leverages a genetic algorithm to automatically optimize the neural network's structure and parameters, effectively overcoming the tendency of traditional BP neural networks to fall into local minima. This significantly improves the model's convergence speed and prediction accuracy. Moreover, the GA-BP model can directly learn nonlinear mapping relationships from complex monitoring data without relying on cumbersome physical parameter modeling, making it well-suited for highly heterogeneous geological environments. As a result, it enhances the accuracy and generalization capability in identifying piping channels. Compared with traditional methods, the GA-BP model demonstrates stronger applicability and practical value, enabling more timely and accurate monitoring and early warning of piping hazards in embankments.

2 Model characterization methods

2.1 Principle of the GA–BP neural network

BP neural networks are widely used multilayer feedforward neural networks that are trained via the error backpropagation algorithm[29-31]. The GA-BP neural network integrates a GA to optimize the initial weights and thresholds of a BP network through selection, crossover, and mutation operations, thereby effectively avoiding the risk of falling into local minima. This method enhances the training performance of the BP neural network by globally optimizing the initial parameters. The specific process is as follows:

(1) BP Neural Network Section

First, the numbers of nodes in the input, hidden, and output layers of the BP neural network are determined based on the task requirements, and the initial weights and thresholds are set randomly to generate an initial solution space. The GA is then employed to optimize these parameters and find the best network configuration. Next, performance criteria are established as the stopping condition for training. During training, forwards

propagation is performed to computes the predicted results, and backpropagation is performed to adjusts the parameters. Finally, the network error is checked to determine whether it meets a predefined threshold. If the error is within the acceptable range, the final prediction results are output; otherwise, training continues until a stopping condition is met.

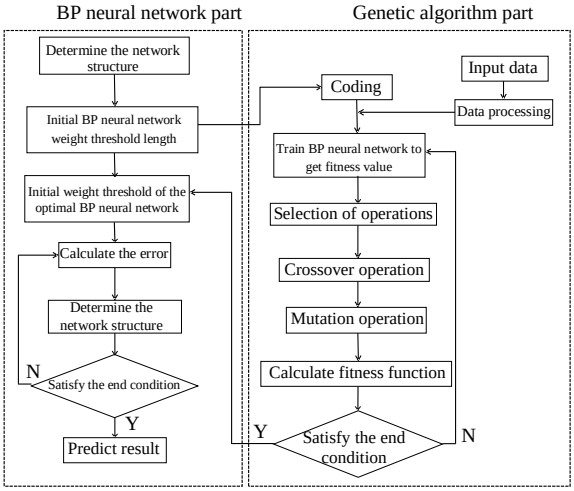


Fig.1 Flowchart of BP neural network based on GA

(2) GA Section

First, the problem data are preprocessed to ensure that they meet the optimization requirements of the GA. Next, the weights and thresholds of the BP neural network are encoded into genes, and the fitness value is evaluated by calculating the network error, which serves as the basis for optimization. Then, based on the fitness values, elite individuals are selected for the next generation, and a genetic crossover operation is performed to generate new candidate solutions. Some individuals undergo genetic mutations to increase the diversity of the solutions. The subsequent steps involve recalculating the fitness values and updating the optimal individuals. If a termination condition is met (e.g., the generation limits has been reached or the fitness has converged), the optimal solution is output. Otherwise, the genetic cycle continues for further optimization.

2.2 Model dataset construction method

The adopted method is a numerical simulation approach for backward erosion piping (BEP) in heterogeneous aquifers. It considers advection to be the dominant mechanism in the BEP process. Therefore, the convective-diffusion equation is simplified by neglecting the diffusion term, resulting in the BEP model as follows:

$$\nabla \cdot (\boldsymbol{K} \nabla h) = S_s \frac{\partial H}{\partial t} + Q \tag{1}$$

$$\frac{\partial C_m}{\partial t} + \nabla \cdot (\boldsymbol{u} C_m) = I \tag{2}$$

where I is the source term; H is the hydraulic head; S_s is the specific storage; and $\boldsymbol{u}$ is the seepage velocity vector of the fluid; C_m is the concentration of mobile particles in the fluid phase; $\boldsymbol{K}$ is hydraulic conductivity coefficient.

The source term I is defined as:

$$I = \begin{cases} \alpha C_r \dfrac{u_a - u_c}{u_c}, & u_a \geqslant u_c \\ \beta C_m \dfrac{u_a - u_c}{u_c}, & u_a < u_c \end{cases} \tag{3}$$

where α and β are empirical coefficients that control the transformation rate between solid-phase mobile particle concentration (C_r) and fluid-phase mobile particle concentration (C_m); u_a is the local seepage velocity; and u_c is the critical velocity threshold.

Equation (3) indicates that when the local velocity exceeds the critical velocity u_c, particle concentration in the solid phase (C_r) begin to convert into mobile particle concentration in the fluid phase (C_m). Conversely, when the flow velocity drops below the critical threshold, mobile particles in the fluid phase tend to settle and convert back into the solid phase.

This method allows dynamic simulation of the piping process and has been validated in the study by Liang et al.[32], titled numerical simulation of backward erosion piping in heterogeneous fields.

2.3 Model building and optimization

To evaluate the effectiveness of the GA-BP network model in representing BEP channels, the hydraulic head (H) and permeability coefficient (K)in the seepage field are selected as training data through the aforementioned dataset construction method. Additionally, to incorporate erosion effects and spatial position, coordinate information (X, Y) is included. Based on the principle of equipotential lines convex to the water flow direction, the head at each X-axis position is categorized and labelled with integers from 0 to 3 to create the head feature (L_H). Thus, the input data consist of H, X, Y, and L_H, while the output data are K. The dataset is then divided randomly into a training set (80%) and a test set (20%). The specific parameter settings are as follows:

(1) GA section

The initial population size is set to 50, with the number of generations set to 50 and variable boundaries range is [–1, 1]. For gene encoding, floating-point encoding with a precision of 1×10^{-6} is used. The selection operation employs the roulette wheel method, with a crossover probability of 0.7 and a mutation probability of 0.05. The root mean square error (RMSE) is used as the fitness function for GA optimization. After multiple rounds of optimization, the optimal individuals are selected, and their genetic codes are reverse-decoded to generate the optimized initial weights and thresholds for the BP neural network.

(2) BP network section

The BP neural network is constructed via the newff function, which consists of three layers: an input layer, a hidden layer, and an output layer. The hidden layer contains 5 neurons, a number determined through multiple trials to balance the model's fitting ability and generalization capability. This configuration effectively captures the nonlinear features in the input data while avoiding overfitting and reduced training efficiency caused by an overly complex network. Before inputting data into the network, the data are first normalized via the mapminmax function to eliminate the effects of dimensionality and outliers. The tangent sigmoid function (tansig) is subsequently used as the activation function from the input layer to the hidden layer. This function has strong nonlinear mapping capabilities with an output range of [–1, 1], which helps enhance the network's ability to represent complex nonlinear relationships. The output layer uses a linear activation function (purelin) to facilitate regression prediction of continuous variables.

The entire training process is optimized via the trainlm function, which includes the Levenberg-Marquardt (L-M) algorithm. The learning rate (α) is set to 0.001. This value was determined as the optimal balance based on multiple preliminary experiments, ensuring both the stability of the training process and a reasonable convergence speed. A learning rate that is too high may cause training oscillations or failure to converge, while a rate that is too low may result in slow training or getting trapped in local minima. The batch size is determined automatically on the basis of the number of samples, with the mean squared error as the loss function. The maximum number of training iterations is set to 1 000, the error threshold (the minimum error between the predicted and actual values) is set to1×10^{-6}, and the minimum gradient (direction of the objective function descent) is set to 1×10^{-7}. The maximum damping coefficient in the L-M algorithm is set to 1×10^{9}, and the maximum validation check count is 35 (i.e., when the loss function fails to decrease for 35 consecutive checks, training automatically stops). The training process terminates automatically when any stopping condition is met.

2.4 Model accuracy assessment metrics

In this study, the mean absolute error (MAE) and mean bias error (MBE) are used as evaluation metrics to quantify the difference between the true and characterized values. Additionally, the RMSE is used to evaluate the magnitude of the characterization error, and the correlation coefficient (R^2) reflects the linear relationship between the true and characterized values.

3 Laboratory BEP test

3.1 Experimental setup

To obtain a dataset suitable for validating the reliability of the GA-BP model, a laboratory sandbox experimental device was designed (Fig. 2) to simulate the BEP and observe its process as well as the formation of piping channels. The device consists of an experimental sandbox, an upstream water supply system, a downstream water collection system, and a water head monitoring system.

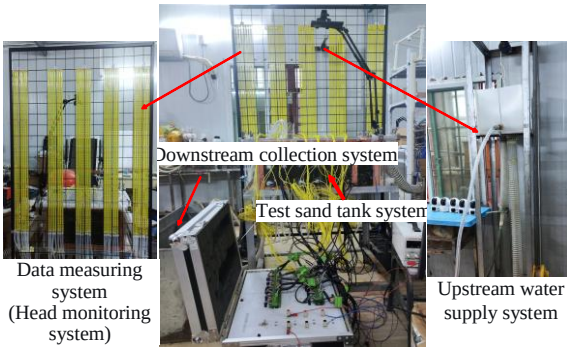


Fig.2 Diagram of the indoor BEP test setup

As shown in Fig.3, the laboratory sandbox has external dimensions of 60 cm × 40 cm × 30 cm × 1 cm (length × width × height × thickness) and is constructed from transparent acrylic panels, which facilitates the observation of fine particle movement and the development of piping channel. The sandbox consists of a top cover plate and a test tank. Six anti-pressure ribs are installed on the exterior to prevent deformation caused by water pressure, and a metal support is mounted on the bottom to ensure a level position. The sandbox is divided internally into a left piping development area and a right filtration area. The filtration area, which measures 10 cm in length, is connected to an inlet pipe on one side and separated from the sample with a sand filter plate on the other side, with gravel fill to stabilize upstream water flow. The piping development area, which measures 50 cm in length, contacts the rubber layer and the cover plate at the top. Thirty-five pressure-measuring pipes (number is A1-A7, B1-B7, C1-C27, D1-D7, E1-E7. Each with an inner diameter of 5 mm, an outer diameter of 7 mm, and a height of 25 cm, with mesh-wrapped ends) are arranged in the central section to measure the water head, with connections to flexible tubing through openings at the bottom.

The upstream water supply system consists of a support frame and a water supply tank. The frame is 2.5 m in height and is equipped with a fixed pulley, a winch, and hemp rope to adjust the water head height. The water supply tank comprises an inner tank and an outer tank. The inner tank, cube with a side length of 25 cm, has an inlet and outlet at the bottom (each with a diameter of 6 cm). The outer tank (a cube with a side length of 30 cm)has an overflow pipe at the top with a diameter of 2 cm. By adjusting the inlet and overflow, a constant water level can be maintained in the inner tank, which allows for a gradual adjustment of the upstream–downstream water head difference.

The downstream collection system consists of a 100 cm× 30 cm×50 cm collection tank that gathers water and sediment discharged from the piping exit. The collection

tank is equipped with a drainage pipe and a stabilization pipe. The drainage pipe removes water and sediment from the sandbox, and the stabilization pipe diverts overflow from upstream to maintain a stable upstream water level. Two pumps are installed inside the collection tank: When fine sand particles have not yet eroded, the smaller pump circulates water from the exit back to the upstream water supply tank to achieve a recirculating flow and conserve water resources. when fine particles begin to erode, the larger pump is activated to expedite drainage.

The water head monitoring system comprises pressure-measuring tubes, flexible tubing, a support frame, and a camera system. Five groups of pressure-measuring tubes (a total of 35 tubes) are mounted on the support frame to display the internal water pressure height within the sandbox. Each pressure-measuring tube is equipped with a 1 m scale and a floating ball for easy reading. The camera system monitors water level changes in real time and records water head data. During the experiment, the pressure-measuring tubes are connected to ports at the bottom of the sandbox by silicone tubing (with an inner diameter of 6 mm and an outer diameter of 10 mm). After the sandbox is filled with water, air is expelled from the tubes, which enables accurate water head measurement. The total water head height is calculated as the sum of the tube height and position height; if the water head exceeds the 1 m measurement range, the support frame height can be adjusted to extend the measurement range.

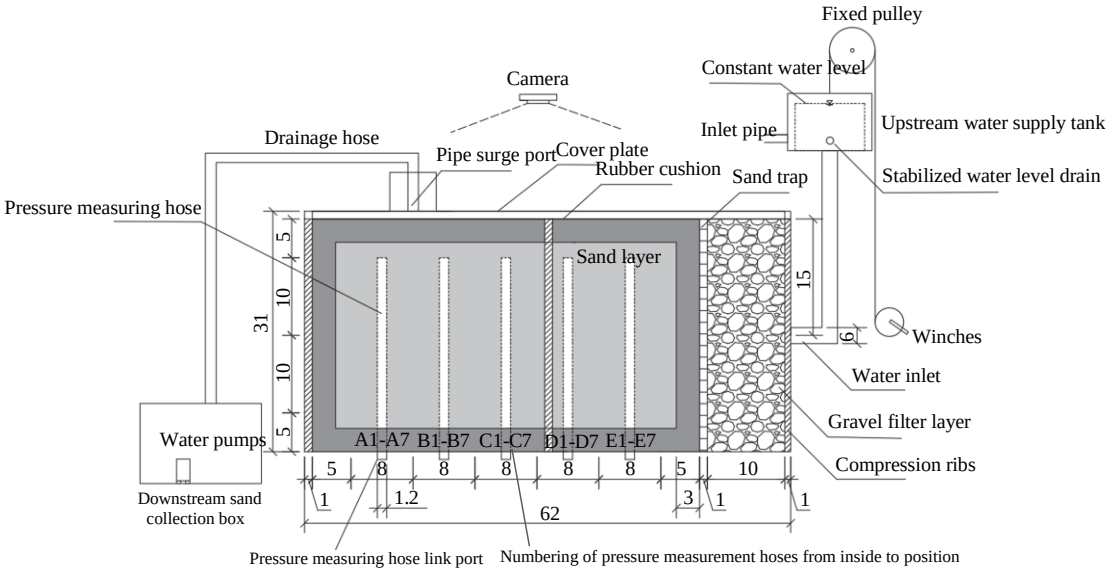


Fig.3 Design of the indoor sandbox test setup (unit: cm)

3.2 Experimental procedure

In the experiments conducted in this study:

1) The first step involved inspecting the sealing of the device to ensure that the sandbox and pipeline connections were leak-free by passing water through the device; this was accomplished by allowing water to flow, confirming that the water column in the pressure pipes rose and remained at a constant height, and verifying that the water supply system could sustain a constant water level.

2) The second step involved preparing the sample. The soil particles were sieved to isolate coarse particles (with sizes from 9 to 12 mm) and fine particles (with sizes from 0.1 to 0.355 mm), which were then thoroughly mixed to create the sample. The particle size distribution of the mixture is shown in Fig. 4. The coefficient of uniformity (C_u) of the mixture was 126.97, and its coefficient of curvature (C_c) was 0.038. According to studies on the effects of particle grading on piping mechanisms[33-35], this sample exhibited internal instability, thereby meeting the conditions necessary for piping initiation.

To ensure that the sample was consistently compacted, the material was loaded into the sandbox in layers. Each layer was approximately 10 cm thick. The mixture was compacted to a specified density before the next layer was added. A rubber bedding layer was laid, and pressurized bolts were used to fasten the cover plate to the sandbox while ensuring that the top of the upstream water supply tank was level with the sandbox. Water was introduced into the sandbox until it covered the top surface of the sample. The sample was saturated for 24 hours to expel trapped air, and the pressure hose tee tube was opened to release air from the water column. The pressure hose and sandbox cameras were activated to record the water level and the development of the pipe surge process continuously. At the beginning of the test, the water tank was gradually raised to control the upstream water level, with a water level increase rate of 3–6 cm per step. When visible particle movement occurred in the sandbox, the raising of the water level was immediately stopped; it was resumed after stabilization, and this process continued until channel development ceased or the test was manually terminated based on the upstream distance.

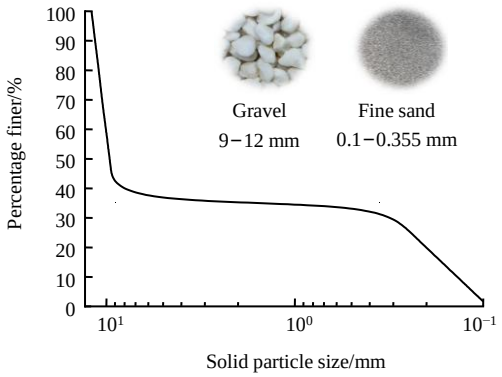


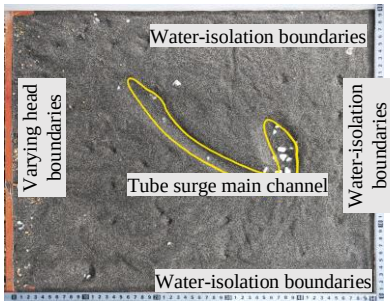
Fig.4 Particle gradation curve

3.3 Experimental results and analysis

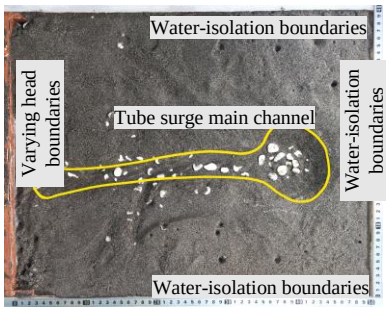
The experimental results of the four BEP tests are presented in Fig. 5, illustrating the development of main seepage channels and revealing the evolving erosion patterns and flow–soil interactions under varying hydraulic gradients. In all tests, the main channel initiates near the downstream piping exit and extends upstream against the flow direction (Fig.5(a)–(d)), demonstrating a retrogressive erosion mechanism where concentrated flow and pressure release at the piping exit mobilize fine particles first, allowing the channel to propagate upstream along the path of least resistance. As erosion progresses, the main channel becomes straighter, wider, and more stable, exposing coarse particles along its boundaries while fine particles are largely washed away (Fig.5(b)). This reflects selective erosion, where fine particles are preferentially removed leaving a coarse-grained skeleton; additionally, trumpet-shaped expansions near the piping exit in some tests indicate localized seepage concentration and increased head loss. Soil heterogeneity induces channel deviations observed in some tests, resulting in curved or S-shaped trajectories (Fig.5(c)), which are attributed to variations in density or particle distribution that disturb seepage paths and cause lateral shifts or branching. The wider distribution of coarse particles around these channels suggests intensified particle sorting and localized flow instability. Notably, the fourth test displays a spoon-shaped channel morphology, with the handle extending toward the upstream head boundary and the bowl near the piping exit (Fig. 5(d)), The "spoon handle" points towards the upstream water head boundary, while the "spoon body" develops near the pipe outlet, indicating localized scour cavities possibly caused by sudden material instability or collapse of supporting structures, and representing an advanced stage of retrogressive erosion. In the experiment, *T* refers to the duration (s) from the beginning of the experiment to the stable formation of the main channel of the piping, and is a key parameter that characterizes the development rate of the piping.

3.4 Dataset construction

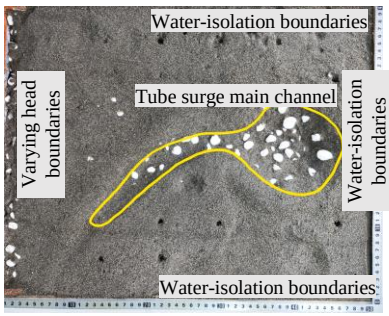
To construct the dataset, four BEP tests were conducted by using the previously described laboratory sandbox, and data such as time *T*, upstream head, measured head, and critical hydraulic gradient date were recorded.



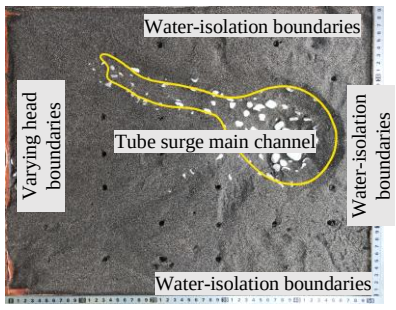
(a) Group I (T=75) main channel boundary diagram



(b) Group II (T=84) main channel boundary diagram



(c) Group III (T=86) main channel boundary diagram



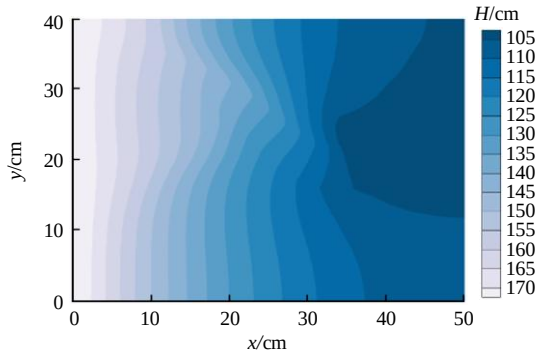
(d) Group IV (T=84) main channel boundary diagram

Fig. 5 Main channel diagram for the BEP test

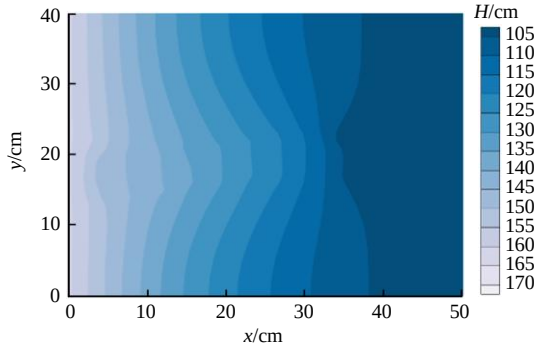
In the numerical simulation of BEP in heterogeneous aquifers, the downstream boundary was set as a varying head, whereas the other boundaries were defined as water isolation boundaries. The coordinates of the piping exit were (37, 20), with an initial head value of 100 cm, an initial permeability coefficient *K* of 0.0016 cm/s, a movable particle ratio of 0.1, a sediment particle ratio of 0.05, and a critical hydraulic gradient of 0.032. Changes in *K* indicate that areas with low permeability represent

regions unaffected by pipe surge damage, whereas areas with high permeability correspond to damaged regions.

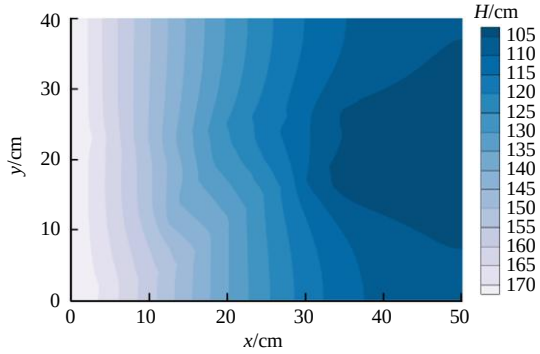
Figs. 6 and 7 show the results of the BEP test. A comparison between Fig. 5 and Fig. 7 reveals that the location, size, and permeability values of the high-permeability zone align with the test results for the piping



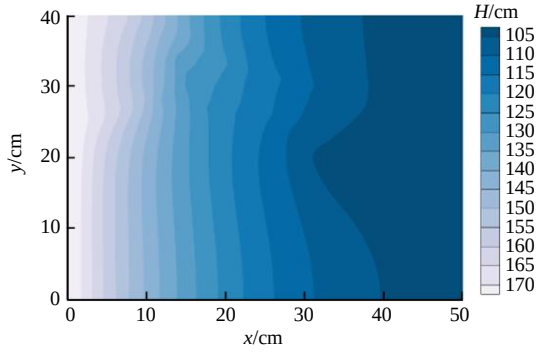
(a) Head field in Group1 (T=75 s)



(b) Head field in Group 2 (T=84 s)

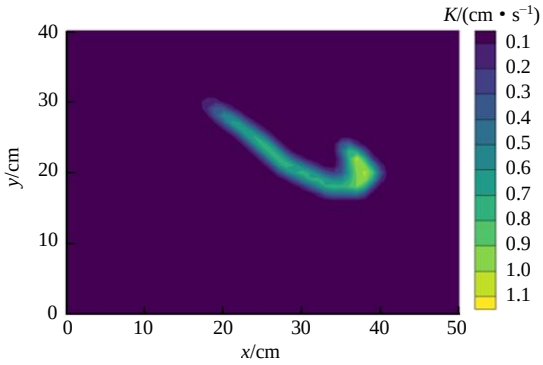


(c) Head field in Group 3 (T=86 s)

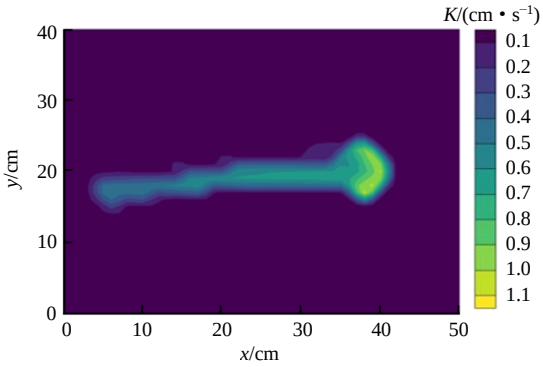


(d) Head field in Group 4 (T=84 s)

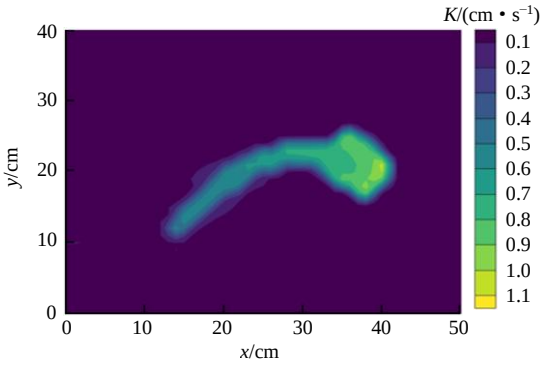
Fig. 6 Head distribution field maps obtained in the simulation experiment



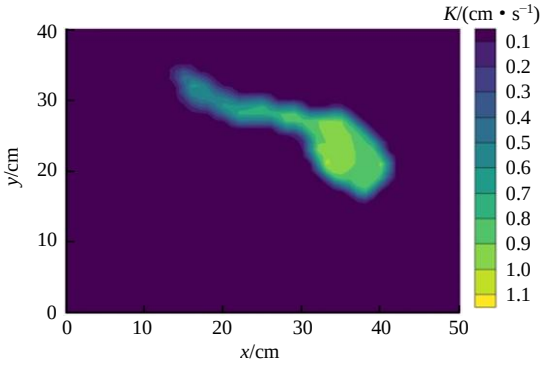
(a) K field in Group 1(T=75 s)



(b) K field in Group 2(T=84 s)



(c) K field in Group 3 (T=86 s)



(d) K field in Group 4 (T=84 s)

Fig. 7 Simulated test *K* field

channel; this indicates that the dynamic model performs effectively. The numerical simulation method for the BEP channel in heterogeneous aquifers can accurately extract the distribution fields of Water head and permeability

coefficient in the piping channel. The dataset is reliable and suitable for use in neural network training.

3.5 Comparison of prediction results between BP and GA-BP

To compare the performance of the BP network and the GA-BP network in K prediction, both models were used to predict the permeability coefficient field of Test Group I at (T=75 s), and the results are presented in Fig. 8. As shown in the figure, the high-permeability regions predicted by both models closely match the actual high-permeability regions in overall spatial distribution, indicating that both models are capable of identifying the location and development patterns of piping channels.

A comparison between Fig.7(a) and Fig. 8 reveals that both the BP and GA-BP networks perform well in characterizing low-permeability regions and capture the general shape and extent of the high-permeability zones, which are consistent with the actual results of Test I (T=75 s). However, some discrepancies remain, particularly in the peripheral contours. The red box in Fig. 8 highlights a region below the upward piping channel where erosion damage is predicted, whereas this phenomenon does not appear in the actual distribution shown in Fig.7(a). In contrast, the corresponding region in Fig.8(b) is smaller in scale and more closely resembles the real condition.

Additionally, the red elliptical area indicates that both models exhibit deviations in predicting the location of the piping exit. These include underestimation of permeability values, smaller predicted exit sizes, and larger angles between the channel and the exit. However, compared with the BP network, the GA-BP network yields more refined results in this region, showing higher permeability values, richer stratified variation, and clearer bifurcation features of the piping channel.

Overall, the GA-BP network demonstrates higher accuracy and better capability in capturing fine details in the spatial distribution of the permeability coefficient.

Since the network is trained using a randomly shuffled dataset and the network itself has inherent randomness, the training results may vary after each training session. To more scientifically evaluate the prediction performance of the BP network and GA-BP network models, both models were subjected to a five-fold cross-validation strategy to assess the generalization ability of the neural network models. In each fold, four subsets were selected as the training set, and the remaining subset was used as the validation set. This process was repeated five times, and the average performance metrics across all folds were calculated to evaluate the model's prediction accuracy and stability. The network settings were consistent with those described earlier, and the evaluation parameters are shown in Table 1.

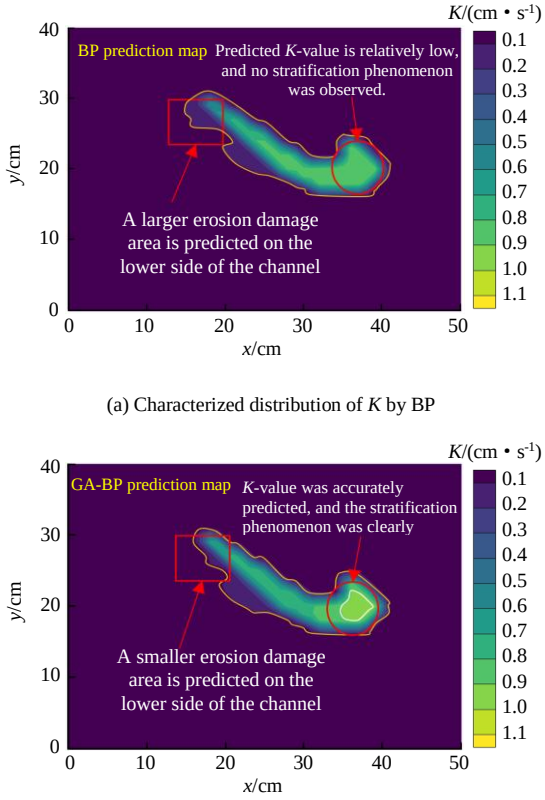


Fig. 8 Predicted permeability fields for test 1 (T=75 s) using neural network models

As shown in Table 1, the GA-BP model outperforms the BP model in terms of prediction accuracy, stability, and generalization ability. The average R^2value for the test set is 0.952, and the MAE, MBE, and RMSE are significantly lower than those for the BP model, indicating that the prediction results are more accurate. The smaller standard deviations of the evaluation metrics further suggest that the model is more stable and robust. Additionally, GA optimization effectively avoids the issue of local optima, improving the convergence speed and prediction consistency of the model, thus demonstrating stronger generalization capability.

Table 1 Prediction Accuracy Evaluation of BP Network and GA-BP Model

Method	Dataset	R^2	MAE	MBE	RMSE
BP	Training set	0.938 (±0.008)	0.0101 (±0.001)	0.0019 (±0.0001)	0.0369 (±0.002)
	Test set	0.932 (±0.015)	0.0112 (±0.001)	0.0019 (±0.0001)	0.0366 (±0.002)
GA–BP	Training Set	0.953 (±0.007)	0.0086 (±0.001)	0.0010 (±0.0006)	0.0347 (±0.003)
	Test set	0.952 (±0.008)	0.0089 (±0.0006)	0.0016 (±0.0001)	0.0356 (±0.002)

Note: The data in the table represents the average values from five runs (±standard deviation).

Based on the above analysis, the GA-BP model outperforms the traditional BP network in terms of accuracy, stability, and generalization ability. Therefore, we have selected the GA-BP model as the core algorithm for predicting permeability coefficients and applied it in subsequent research.

4 Effect of the dataset on the accuracy of the GA-BP model

4.1 Scheme design

In dynamic simulations of BEP, the data from the pipe surge damage phase exhibit greater variability but account for a smaller proportion of the dataset. This imbalance negatively impacts the model's ability to accurately characterize changes in permeability coefficient, particularly in high-permeability regions, where characterization deviations are more pronounced. The application of under sampling to reduce the amount of data with minor permeability coefficient changes risks the loss of critical information, whereas oversampling data with substantial changes can introduce noise and undermine model stability. To address this issue, simulated data from Groups II, III, and IV tests were incorporated to augment the dataset, and the effect of dataset quality on the characterization accuracy of the GA-BP network model was examined. The design of the training schemes is detailed in Table 2, where the proportion of data that exhibited significant permeability coefficient changes increased progressively across the three groups, thereby improving the dataset quality.

4.2 Analysis of the results

The data used to evaluate the different schemes are provided in Table 3. The results of the fitness function are shown in Fig.9, a comparison of the network characterization results for each scheme is depicted in Fig.10, and the variation in the loss function across different schemes is presented in Fig.11. As shown in Table 3, after dataset optimization, R^2 for Schemes 1 to 3 increased from 0.95 to 0.96, the MAE decreased from 0.009 to 0.008, the MBE decreased from 0.016 to 0.015, and the RMSE decreased from 0.035 to 0.032. Although the evaluation parameters changed slightly, the characterization accuracy improved as the proportion of data with larger changes increased; this suggests that a more balanced and comprehensive dataset results in higher characterization accuracy of the network model.

Table 2 Design of the training scheme for different datasets

Scheme	Number of training sets	Data source	Rapidly varying K samples		Characterization results
			Percentage of data/%	Number of data groups	
1	2 000	II (T=84 s)	20.3	406	
2	4 000	II (T=84 s), III (T=86 s)	21.2	848	Test I (T=7s5): (H, X, Y, L_H; K)
3	6 000	II (T=84 s), III (T=86 s), IV (T=84 s)	22.6	1 356	

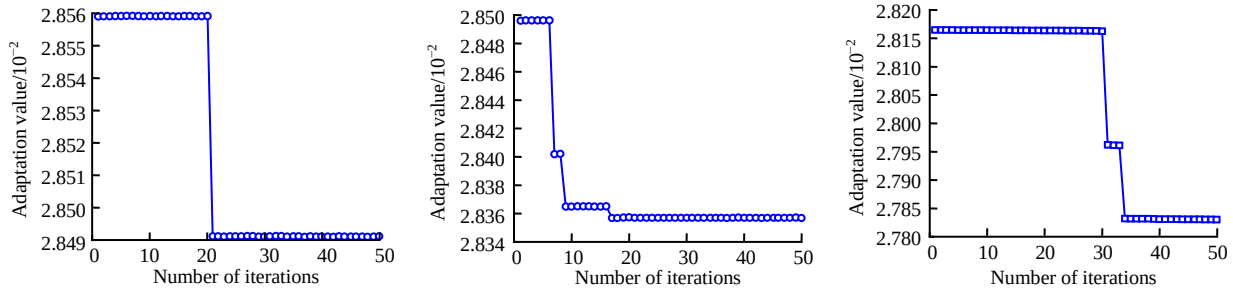
As shown in Fig. 9, the fitness function for each scheme stabilized around the 20th iteration. As the proportion of data with significant K changes increased, the stabilized fitness value decreased from 0.028 49 in Scheme 1 to 0.027 83 in Scheme 3, which suggests that higher dataset quality improves the accuracy of the GA algorithm.

As shown in Figure 10, reveals a clear dependency between the predicted and actual permeability values; specifically, the prediction errors exhibit structured variation across different permeability ranges. For samples with $K \leqslant 1.0$ cm/s, the model exhibited high accuracy with minimal deviations. In contrast, when K>1.0 cm/s, the prediction errors increased systematically, and the model consistently underestimated the permeability values. This phenomenon is particularly evident in Fig. 10(a) and 10(b), which is primarily attributed to the limited training data and the low proportion of high-permeability samples in Scheme 1. Such data imbalance hinders the model's ability to adequately learn from minority samples, thereby impairing its generalization and robustness. As the data volume increased and the proportion of high-permeability samples rose in Scheme 2 (Figs. 10(c) and 10(d)) and Scheme 3 (Figs. 10(e) and 10(f)), the dependency was partially alleviated. However, it was not completely eliminated, indicating that the model continues to exhibit underfitting and a delayed response when confronted with extreme high-permeability conditions. This systematic error dependence underscores the non-random nature of the prediction bias and highlights the critical importance of training data distribution in achieving robust model performance.

Table 3 Data for assessment of the characterization accuracy of different schemes

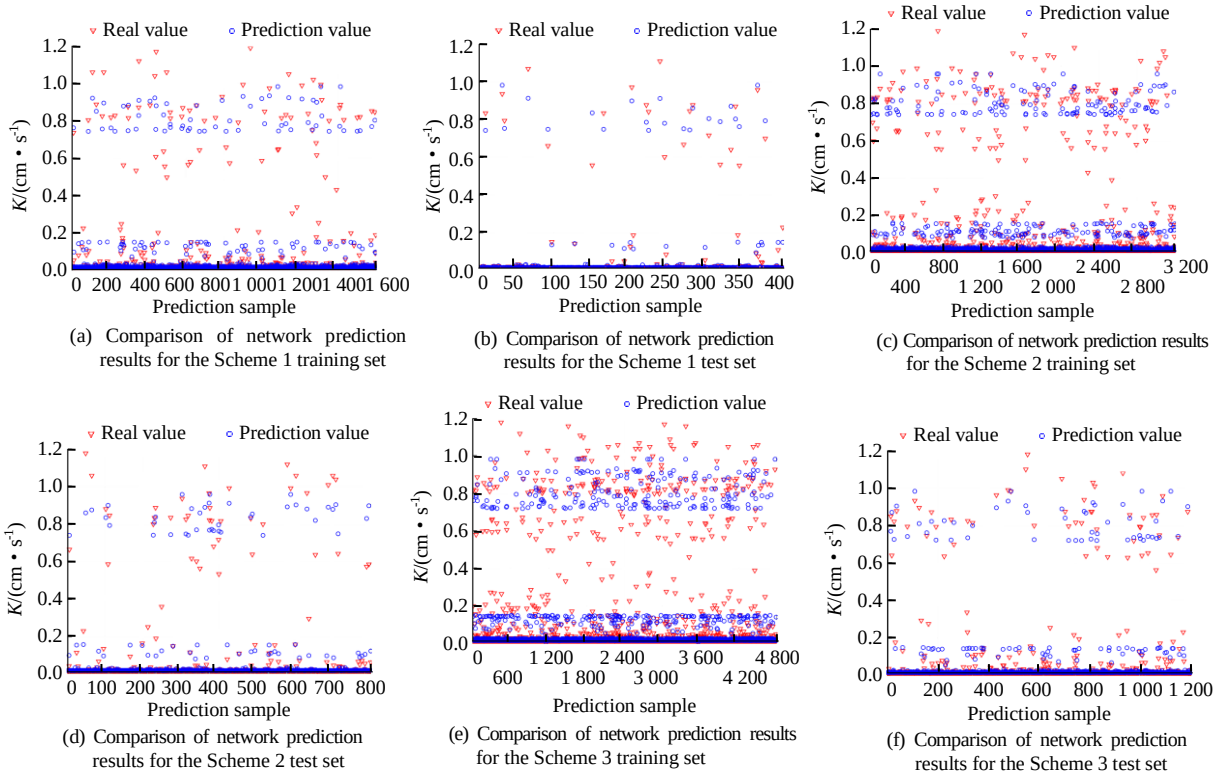
Scheme	Assessment indicators - training set				Evaluation metrics - test sets			
	R^2	MAE	MBE	RMSE	R^2	MAE	MBE	RMSE
1	0.95052	0.0091052	0.0016252	0.035973	0.94805	0.0088107	0.0016876	0.035757
2	0.95757	0.0084059	0.0016041	0.033833	0.95816	0.0083410	0.0016507	0.034884
3	0.96129	0.0080896	0.0015040	0.032518	0.96165	0.0081422	0.0014860	0.032628

Figure 11 shows the convergence curves of the loss functions for each scheme during the training process. From the figure, it can be seen that all three schemes can effectively converge to a lower level. Based on the more comprehensive accuracy evaluation indicators (R^2, MAE, MBE, RMSE) in Table 3, it can be seen that Scheme 3 achieved the best comprehensive performance on both the training and testing sets, with the highest representation accuracy.



(a) Scheme 1 adaptation change curve (b) Scheme 2 adaptation change curve (c) Scheme 3 adaptation change curve

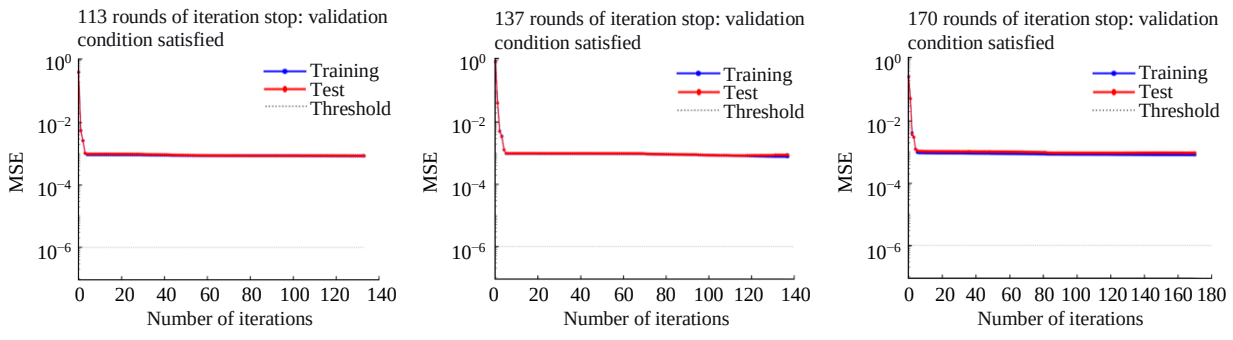
Fig. 9 Fitness functions for different schemes



(a) Comparison of network prediction results for the Scheme 1 training set (b) Comparison of network prediction results for the Scheme 1 test set (c) Comparison of network prediction results for the Scheme 2 training set

(d) Comparison of network prediction results for the Scheme 2 test set (e) Comparison of network prediction results for the Scheme 3 training set (f) Comparison of network prediction results for the Scheme 3 test set

Fig. 10 Comparison of network prediction results for different schemes



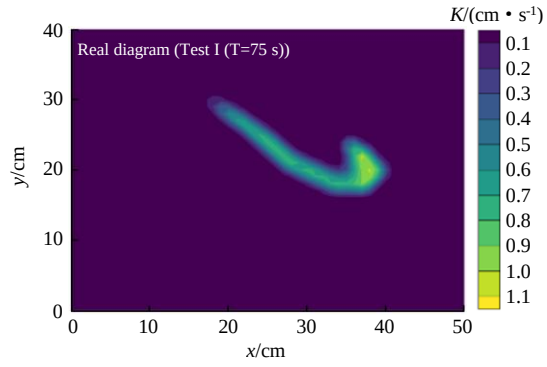
(a) Loss function for Scheme 1 (b) Loss function for Scheme 2 (c) Loss function for Scheme 3.

Fig. 11 Loss functions for different schemes

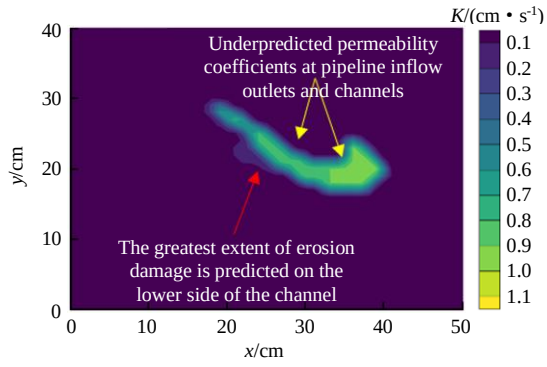
4.3 Analysis of results

Network models trained on different schemes were applied to characterize the K distribution for Test I (T=75 s). The actual and characterized plots are shown below.

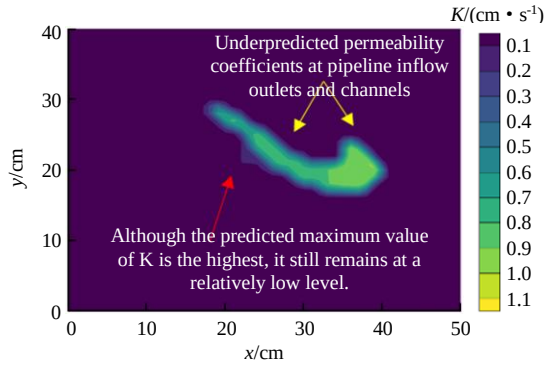
Figs. 12(a) to 12(d) demonstrate that all three schemes characterized the approximate location and morphology of the BEP channel. As the dataset quality improved, the erosion area on the lower side of the channel, which is marked by red arrows, gradually decreased, whereas the permeability coefficient within the channel, which is highlighted by yellow arrows, gradually increased, particularly at the channel centre, piping exit, and bifurcations. A comparison of Fig. 12 (b)-12(d) with 12(a), reveals the results. The characterized erosion area on the lower side of the channel gradually decreased across the three plans. The characterized permeability coefficient also increased accordingly at the piping exit and within the channel.



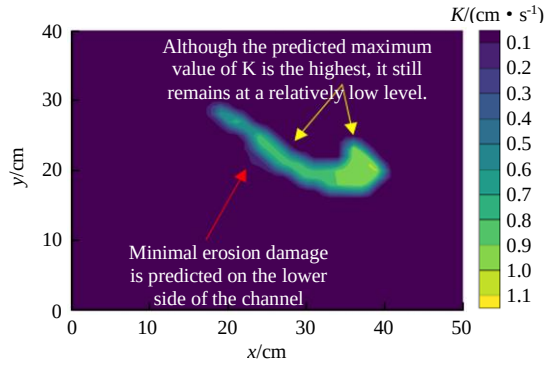
(a) Characterized distribution of permeability coefficient for Test I (T=75 s)



(b) Characterized distribution of permeability coefficient for Scheme 1



(c) Characterized distribution of permeability coefficient for Scheme 2



(d) Characterized distribution of permeability coefficient for Scheme 3

Fig. 12 Characterization of the permeability coefficient field for Test I (T=75 s) by different schemes

Although Scheme 3 demonstrated better characterization performance, the permeability coefficients at the channel centre, piping exit, and bifurcations remained insufficient, and stratification details were still lacking. These prediction errors may arise from the following aspects: (1) Uneven data distribution. Samples from high-permeability areas are scarce, causing the model training to focus more on overall error and resulting in insufficient fitting accuracy in these regions; (2) Limitations of the model structure. The BP network is suited for continuous and smooth function mapping, whereas high-permeability areas exhibit abrupt changes and strong nonlinearity. Although GA optimization improves the initial weights, its ability to represent extreme values remains limited; (3) Experimental error interference. The measurement of permeability coefficient is significantly affected by disturbances and fluctuations in the water head, especially in high-permeability zones where flow velocity is high and fluctuations are large, which amplifies measurement errors and impacts the model's true learning from the data.

Overall, the characterization performance of the GA-BP network model improved as the proportion of data with significant changes in permeability coefficient increased, and as the dataset became more balanced and comprehensive.

5 GA-BP model imaging characterization and analysis of the results

Using 6 000 datasets from Scheme 3 and the optimized GA-BP network model, the BEP channels were predicted and characterized (Fig. 13). At the end of the experiment, the water pressure and positional head values from each piezometer were recorded, which provided input data for estimating permeability coefficient for the surface layer of the sand sample. These inputs were processed by the GA-BP network model to predict permeability coefficient, and the results were visualized. The input head data are shown in Fig. 14, and the predicted field of permeability coefficient is presented in Fig. 15.

A cloud diagram of the permeability coefficient distribution reveals that the development trend of the BEP channel, which is indicated by the high seepage area, is generally consistent with the test results, although notable

deviations exist in the size and extent of the channel. The value of permeability coefficient in the main channel is greater than those in areas unaffected by BEP, which aligns with the actual conditions. The value of permeability coefficient at the piping exit is higher and ranges from 0.5 to 1.0 cm/s, whereas those in the upstream channel are lower, between 0.5 and 0.8 cm/s, thus indicating poor characterization accuracy for the upstream channel. Although the characterization results include points with permeability coefficient $K \geqslant 1.1$ cm/s, they do not form a centralized distribution in the cloud diagram. Additionally, the cloud maps display a certain range of scours around the piping channel, but the scour areas of the branch channel and inlet are not characterized.

To better quantify the extent of the piping channel, dimensional data from Figs.13 and 15, defined by a boundary of 0.5 cm/s, are recorded in Table 4. The results indicate that the scour area of the piping channel extends from x: 28.96 to 43.23 cm and y: 15.73 to 30.14 cm, whereas the scour area of the upstream channel spans from x: 2.51 to 28.96 cm and y: 22.71 to 29.05 cm. The offset distance between the centre of high seepage and the deepest point is 3.63 cm. Compared with the actual erosion dimensions, the GA-BP network model resulted in a longer and narrower piping exit, whereas the upstream channel is shorter and narrower. Additionally, the centre of high seepage is offset significantly from the centre point, which leads to notable deviations in the overall dimensions of the main channel.

In predicting piping channels using the GA-BP neural network, while the overall development trend is accurately captured, there are still deviations in the location, scale, and local features of the channels. For example, the predicted channel shape is inaccurate, high-permeability regions are misaligned, and shallow erosion areas are inadequately identified. These issues may arise from several limitations: 1)The model has difficulty accurately characterizing high-permeability regions; 2)Model validation is currently based on only four sets of experimental data, with limited coverage of soil conditions, hydraulic gradients, and particle size distributions, thereby restricting the model's generalization capability; 3)Although the study compares the GA–BP model with the traditional BP model, it lacks comparative analysis with other advanced machine learning methods, which should be addressed in future research; 4) Applying the model under large-scale field conditions poses significant challenges, including increased environmental complexity, greater difficulty in data collection, and the complexity of spatiotemporal variability. To address these challenges, the following improvements are proposed:

(1) Increase the number and density of pressure sensors and use Kriging or Inverse distance weighted (IDW) interpolation to extend head data, improving spatial coverage.

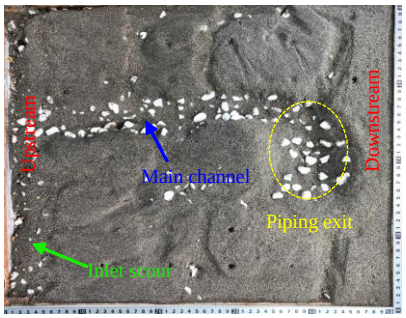


Fig. 13 Reverse erosion channel map for the original test

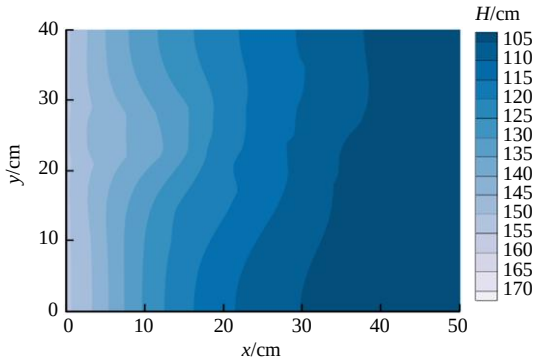


Fig. 14 Map of head field to be input

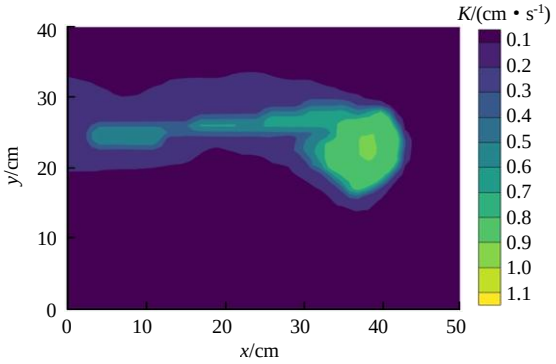


Fig. 15 Network characterization of permeability coefficient for actual BEP channel

(2) Introduce high-precision optical fiber sensors, wireless pressure sensors, or distributed monitoring systems, combined with image monitoring and other multi-source data fusion techniques, to enhance data quality and measurement accuracy.

(3) Apply convolutional neural networks (CNN) to better process spatial distribution features of the permeability coefficient and, combined with GIS data, more accurately describe channel morphology.

(4) Integrate long short-term memory (LSTM) networks with the GA-BP model, using time series data augmentation techniques to improve the model's ability to learn the temporal evolution of the seepage process.

(5) Expand the experimental dataset to include a wider range of soil conditions, particle size distributions, and hydraulic gradients, thereby enhancing the model's generalization capability.

Table 4 Comparison of the main channel sizes from the network model imaging results

Part	Position	True Range	Characterized range	Actual erosion size/cm	Characterized erosion size/cm	Deviation/cm	Result
Piping exit	*x*	34.9−45.3	28.96−43.23	10.4	14.27	3.87	Too long
	y	11.5−29.0	15.73−30.14	17.5	14.41	−3.09	Narrow
Upstream channel	*x*	3.0−34.9	2.51−28.96	31.9	26.45	−5.45	Relatively short
	y	22.0−29.7	22.71−29.05	7.7	6.34	−1.36	Narrower
Center point	*x*	40.0	38.01	Offset:3.63 cm			Too far
	y	20.0	23.04				

(6) Conduct model testing under large-scale field conditions to assess its adaptability to complex environments and variable boundary conditions, and continuously optimize the model based on field feedback.

In conclusion, although the model does not fully account for the physical mechanisms of piping and multi-factor coupling, the GA-BP network demonstrates strong predictive capabilities. It can effectively support piping hazard identification and risk assessment, showcasing its potential for engineering applications and practical value.

6 Conclusions

This study focused on BEP under the conditions of a double-layer foundation, and four sets of laboratory experiments were conducted. A dataset was constructed via numerical simulations of BEP in a heterogeneous aquifer and was then compared with the experimental results. Data extracted from the sandbox experiments were used to examine the effects of highly variable data percentages on the characterization accuracy of the GA-BP model. Finally, the optimized model was employed to characterize and delineate the original BEP channel. The main conclusions are as follows:

(1) The permeability coefficient distribution field derived from the numerical simulation of BEP in a heterogeneous aquifer closely resembles the main channel observed in sandbox laboratory tests in terms of shape and size. This similarity suggests that the dataset constructed via this method has high reliability.

(2) During the optimization of the GA-BP network model, three data occupancy schemes were developed to enhance the datasets with significant variations. The results indicated that, for permeability coefficient $K \leqslant 1.0$ cm/s, the deviation between the characterized and true values gradually decreased with increasing dataset size. In contrast, the characterization accuracy for $K > 1.0$ cm/s was inadequate.

(3) The GA-BP network model was used to characterize the BEP channel in laboratory tests, and the model indicated that the piping exit exhibits a long and narrow characteristic, whereas the upstream channel was observed to be both short and narrow, with the hypersepage centre exhibiting a larger offset from the centre point. These observations suggest that the GA-BP network model is capable of effectively characterizing the development trend of the BEP channel; however, discrepancies remain regarding the location and scale of the channel compared with the actual conditions.

In conclusion, this study serves as a valuable reference for characterizing BEP channels and further substantiates the potential of the GA-BP network model in this domain.

References

[1] WU Qing-hua, ZHANG Wei, WU Ai-qing, et al. Progress of research on dike pipe surge risk[J]. Journal of Changjiang River Scientific Research, 2019, 36(10): 39-44.

[2] HAN Xu, LUO Deng-chang. Basic features and application strategy of big data for Yangtze River embankment engineering[J]. Yangtze River, 2020, 51(Suppl.1): 262-264.

[3] VAN BEEK V M, ROBBINS B A. et al. Use of incipient motion data for backward erosion piping models[J]. International Journal of Sediment Research, 2019, 34(5): 401-408.

[4] WANG Z J, OSKAY C, FASCETTI A. Backward erosion piping in geotechnical infrastructure: a rate process perspective[J]. Geotechnique, 2024, 71(2):255-265.

[5] MA Z, WANG X, SHANG N, et al. A new numerical method to evaluate the stability of dike slope considering the influence of backward erosion piping[J]. Water, 2024, 16(12): 1706-1706.

[6] RIHA J, PETRULA L. Experimental research on backward erosion piping progression[J]. Water, 2023, 15(15): 2749-2749.

[7] LIU H C, SU H Z, YANG J Q, et al. Multi-fidelity deep neural network with Monte Carlo dropout technique for uncertainty-aware risk recognition of backward erosion piping in dikes[J]. Applied Soft Computing, 2024, 112: 112-165.

[8] Ministry of Water Resources of the People's Republic of China. China water statistical yearbook 2023[M]. Beijing: China Water & Power Press, 2023.

[9] https://www.thepaper.cn/ newsDetail_forward_27999568 ZHU Yuan-xiang, TAN Jun, CHEN Xu-hou. The beginning and end of the breach of the Dongting Lake levee at Tuanzhou: a 2-hour defeat, a 77-hour "counterattack" [N/OL]. The Paper (2024-07-09) [2024-08-18]. https://www.thepaper.cn/newsDetail_forward_27999568.

[10] PENG S G, RICE J D. Inverse analysis of laboratory data and observations for evaluation of backward erosion piping process[J]. Journal of Rock Mechanics and Geotechnical Engineering, 2020, 12(5): 1080-1092.

[11] LOPERTE A, BAVUSI M, CERVERIZZO G, et al. Ground penetrating radar in dam monitoring: the test case of Acerenza (Southern Italy)[J]. International Journal of Geophysics, 2011(1): 1-9.

[12] ZHANG Jian-qing, XU Lei, LI Peng, et al. Experimental study of integrated physical exploration technology in dam leakage detection[J]. Advances in Geophysics, 2018, 33(1): 432-440.

[13] ZHAO Han-jin, JIANG Xiao-yu, HAN Jun-liang, et al. Experimental study on integrated geophysical methods in the joint diagnosis of seepage in earth-rock dams[J]. Advances in Geophysics, 2021, 36(3): 1341-1348.

[14] GE S L, HU S F, CHEN G X, et al. Characterization of a leaky earth dam using integrated geophysical surveys[J]. Journal of Applied Geophysics, 2023, 215(1): 105099.

[15] QIU H Y, HU R, HUANG Y, et al. Detection and quantification of dam leakages based on tracer tests: a field case study[J]. Water, 2022, 14(9): 1448.

[16] HAMLYN J E, BIRD C L. Geophysical investigation and monitoring of dam infrastructure[J]. Dams and Reservoirs, 2021, 31(2): 57-66.

[17] LIN C H, LIN C P, HUNG Y C, et al. Application of geophysical methods in a dam project: life cycle perspective and Taiwan experience[J]. Journal of Applied Geophysics, 2018, 158: 82-92.

[18] SUN Y D, RU S R. Application of non-destructive testing in reservoir dam safety monitoring[J]. Environmental & Earth Sciences Research Journal, 2022, 9(3): 98-103.

[19] RADZICKI K, STOLIŃSKI M. Seepage monitoring and leaks detection along an earth dam with a multi-sensor thermal-active system[J]. Bulletin of Engineering Geology and the Environment, 2024, 83(9): 1-15.

[20] RANA N M, DELANEY K B, EVANS S G, et al. Application of Sentinel-1 InSAR to monitor tailings dams and predict geotechnical instability: practical considerations based on case study insights[J]. Bulletin of Engineering Geology and the Environment, 2024, 83(5): 204.

[21] RADZICKI K, GOLEBIOWSKI T, CWIKLIK M, et al. A new levee control system based on geotechnical and geophysical surveys including active thermal sensing: a case study from Poland[J]. Engineering Geology, 2021, 293: 110-120.

[22] ZHAI Yue, LIU Lang, YU Shu. Grid search-support vector machine method for identifying the possibility of dike piping occurrence[J]. Journal of Central South University (Science and Technology), 2015, 46(4): 1497-1503.

[23] RAO Xiao-kang, MA Rui, ZHANG Li, et al. Research on safety management platform for dike engineering based on GIS+BIM+IoT digital twin[J]. Rural Water Conservancy and Hydropower in China, 2022(1): 1-7.

[24] LU G Y, OUYANG P, CHENG Y, et al. Intelligent identification method for dike piping monitoring based on YOLO model[J]. Advances in Water Science and Hydropower Engineering, 2024, 44(1): 89-94.

[25] BAND S S, JANIZADEH S, SAHA S, et al. Evaluating the efficiency of different regression, decision tree, and Bayesian machine learning algorithms in spatial piping erosion susceptibility using ALOS/PALSAR data[J]. Land, 2020, 9(10): 346.

[26] DING S F, SU C Y, YU J Z. An optimizing BP neural network algorithm based on genetic algorithm[J]. Artificial Intelligence Review, 2011, 36: 153-162.

[27] CAO M H, NIE Z L, SONG L, et al. GABP-based multiparameter identification for permanent magnet synchronous linear motors[J]. Journal of Power Electronics, 2024, 24(9): 1428-1437.

[28] LI B W, SHEN L G, ZHAO Y, et al. Quantification of interfacial interaction related with adhesive membrane fouling by genetic algorithm back propagation (GABP) neural network[J]. Journal of Colloid and Interface Science, 2023, 640(1): 110-120.

[29] XIE J Y, ZHENG J C, BAI L. Model for restoring obstructed beam transmission in atmospheric turbulence based on BP neural network[J]. Physics Letters A, 2024, 130030.

[30] ZHANG J, LIU L, WANG L, et al. Fault detection of key parts of wind turbine based on BP neural network combination prediction model[J]. Energy Informatics, 2024, 528: 124-124.

[31] LI X N, CHENG X, WU W J, et al. Forecasting of bioaerosol concentration by a back propagation neural network model[J]. Science of the Total Environment, 2020, 698: 134315.

[32] LIANG Y, YEH T C J, WANG Y L, et al. Numerical simulation of backward erosion piping in heterogeneous fields[J]. Water Resources Research, 2017, 53(4): 3246-3261.

[33] NI Xiao-dong, KOU Heng-qi, ZUO Xiang-yu, et al. Research on the microscopic mechanism of piping based on transparent soil technology and particle flow method[J]. Journal of Hydraulic Engineering, 2021, 52(12): 1482-1497.

[34] YAO Zhi-xiong, ZHOU Jian, ZHANG Gang, et al. Experimental study on the influence of particle gradation on piping development[J]. Journal of Hydraulic Engineering, 2016, 47(2): 200-208.

[35] KANG Jie, REN Jie, NAN Sheng-hao, et al. Experimental study and hydraulic condition analysis of piping in sand under shape effect[J]. Journal of Hydroelectric Engineering, 2023, 42(5): 97-106.